Int. J. Electrochem. Sci., 11 **(2016)** 7359 – 7369, doi: 10.20964/2016.09.36

International Journal of
ELECTROCHEMICAL
SCIENCE
www.electrochemsci.org

Corrosion Study of Al-Fe (20 wt%) Alloy in Seawater Alkaline Solutions

J.E. Flores-Chan[1,*], *A. Torres-Islas*[2], *C. Patiño-Carachure*[3], *G. Rosas*[1], *M.A. Espinosa-Medina*[4,*]

[1] Instituto de Investigación en Metalurgia y Materiales, UMSNH, C.P. 58000, Morelia, Mich. México.
[2] Facultad de Ciencias Químicas e Ingeniería Mecánica, Universidad Autónoma del Estado de Morelos. C.P. 62209, Cuernavaca, Morelos, México.
[3] Facultad de Ingeniería, Universidad Autónoma del Carmen, Campus III, Av. Central S/N, Esq. con Fracc. Mundo Maya, C.P. 24115 MSNH, Ciudad del Carmen, Campeche, México.
[4] Facultad de Ingeniería Mecánica, UMSNH, C.P. 58000, Morelia, Mich. México.
[*]E-mail: marespmed@gmail.com, enri_flores@hotmail.com

Received: 30 May 2016 / *Accepted:* 8 July 2016 / *Published:* 7 August 2016

The assessment of corrosion susceptibility of the Al-Fe (20 wt%) alloy in seawater at different alkaline pH values was performed applying potentiodynamic polarization, linear polarization resistance (LPR) and electrochemical impedance spectroscopy (EIS) techniques. The electrochemical results carried out at room temperature showed lower values of the corrosion current density of about 0.008 - 0.0896 mA/cm^2. The polarization curves showed the formation of an unstable layer which decreases with the pH increasing. EIS results revealed a corrosion mechanism controlled by the ion transport through the permeable film. Microstructural characterization confirmed the formation of hydroxides phases as corrosion products by increasing the pH and exposure time.

Keywords: Al-Fe (20 wt%) alloy, electrochemical techniques, seawater.

1. INTRODUCTION

Intermetallic compounds within Fe-rich region in the FeAl phase diagram are considered structural materials due to their attractive physical, chemical and mechanical properties combined with low density and low cost [1-3]. However, the intermetallic compounds in the Al-rich portion such as $FeAl_2$, $FeAl_3$, and Fe_2Al_5 are susceptible to hydrogen environment embrittlement caused by the reaction of the aluminium and the air humidity according to the following reaction [4, 5]:

$$2Al + 3H_2O \rightarrow Al_2O_3 + 6H^+ + 6_e^- \qquad \Delta G = -289 \qquad \text{kJ/mol}H_2 \qquad (1)$$

From the reaction, has been widely discussed that the hydrogen released provokes cleavages fracture of the intermetallic materials. Also, the cleavages fracture is accentuated with the aluminium content in the alloy. It is important to note that hydrogen environment embrittlement is not essentially a corrosion process, but can enhance. Among the above intermetallic compounds, $FeAl_3$ contains the highest Al ratio, so it would be expected that the corrosion process in this intermetallic will increase. In the other hand, with increasing corrosion of the material, a greater amount of hydrogen is released.

In the past, the aluminium and its alloys have been proposed to generate hydrogen from the hydrolysis of water for fuel cells applications. Thus, the intermetallic alloys are also considered candidates for hydrogen generation. A circumstance that assists this purpose is that released hydrogen gas from the reaction minimizes the cohesive forces resulting in the breaking down of the material, and then increasing the surface area of the reaction [6, 7]. However, an important feature for the use of aluminium and its alloys is to remove the oxide layer formed by exposing the aluminium in aqueous media [8, 9]. It is known that the thickness and stability of the passive layer depend on the composition of the electrolyte and electrochemical parameters, such as; corrosion potential, E_{corr}, corrosion density, i_{corr}, pH, etc. [10, 11]. In this way, a continuous film rupture improves efficiency and kinetics of the corrosion process for hydrogen generation. For this propose, the use of $Ca(OH)_2$ addition has been utilized in the past [12-15].

Thus, the aim of this study is to investigate the corrosion process in the Al-Fe (20 wt%) alloy using artificial seawater as the electrolyte. To evaluate the effect of pH on the corrosion rate in the intermetallic alloy the seawater was modified reached to an alkaline region by adding $Ca(OH)_2$ promoter. Therefore, the continuous removal of the passive oxide layer was promoted in the alloy with $Ca(OH)_2$ additive to increase the corrosion rate.

2. EXPERIMENTAL

The Al-Fe (20 wt%) alloy was obtained under conventional gravity casting techniques using high purity elements (99.99 wt%). To reveal the microstructure of the alloy was mechanically polished with emery paper, cleaned, and then chemically attacked with the 2% HBF_4 and 200 mL H_2O solution. Samples were immersed for 5 seconds applying 10 V in DC potential. The samples for the corrosion tests were prepared according to ASTM G31-72 (1.3 x 1.3 x 1 cm^3) standard. Before corrosion tests, the surface of the specimens of each experimental condition was SiC devastated (grade 1500), cleaned with acetone and dried. The corrosive agent was synthetic seawater prepared according to ASTM-D1141-98 standard. To increase the corrosion rate, the pH of seawater was adjusted at 10, 12 and 14 by adding $Ca(OH)_2$, All the reagents used in the seawater preparation were analytical grade.

The electrochemical techniques for corrosion tests were potentiodynamic polarization curves, linear polarization resistance (LPR), and electrochemical impedance spectroscopy (EIS). The tests were performed according to ASTM G5-94, G59-91 and G106-89 standards respectively. The electrochemical cell consisted of three electrodes arrangement; saturated calomel (SCE) as a reference, a graphite bar as a counter electrode and the Al-Fe (20 wt%) alloy samples as working electrode. The arrangement was connected to a potentiostat Gill-AC (ACM Instruments) attached to a computer.

The potentiodynamic test was established in a potential window -1000 to 2000 mV versus the

OCP with a scan rate of 1 mV/s. The values of the corrosion current density are calculated using the Tafel extrapolation method taking an extrapolation zone 150 mV versus OCP. Linear polarization resistance (LPR) measurements were performed in the range of -15 to +15 mV at a scan rate of 1 mV/s recording a measurement every 15 min during 24 h. EIS test was developed by applying an excitation signal of ±15 mV vs. open circuit potential, in the frequency range of 10,000 Hz to 0.01 Hz. All tests were performed at room temperature and in triplicate to ensure reproducibility of the experiments. The morphological and chemical characterization of materials was conducted in an X-ray diffractometer (BRUKER D8 ADVANCE). Scanning electron microscopy (SEM) was carried out on a JEOL JSM-7600F with microanalyzer BRUKER model adapted X-Flash 6130.

3. RESULTS AND DISCUSSION

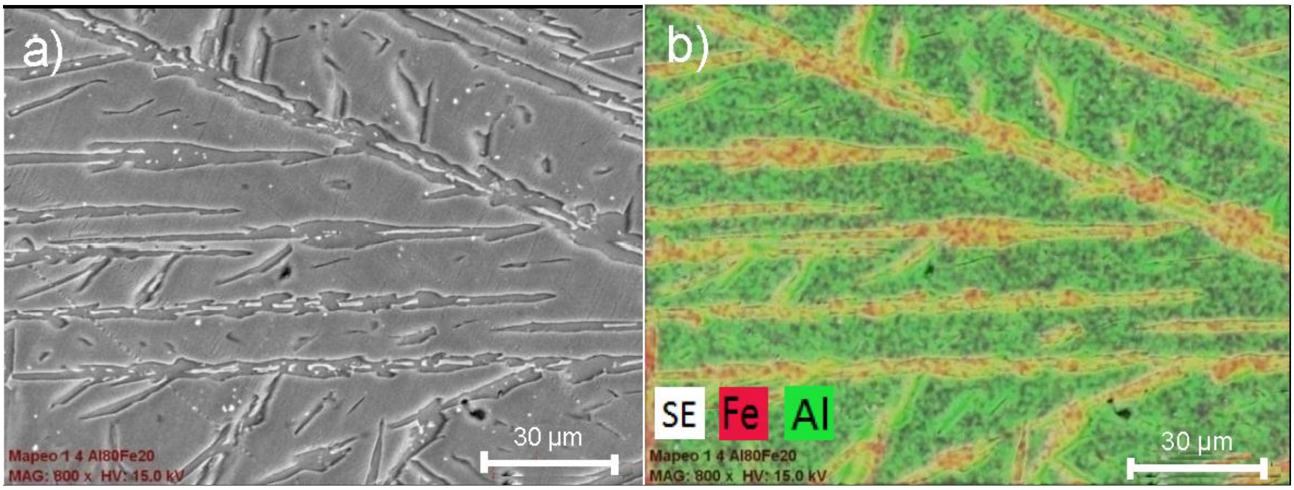

Figure 1. Microstructural characterization of Al-Fe (20 wt%) as-cast alloy: a) SEM micrograph, b) X-ray elements mapping.

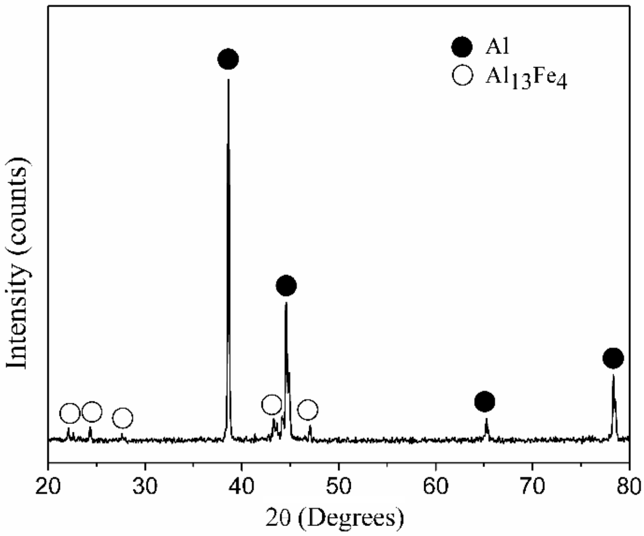

Figure 2. Chemical composition characterizations by XRD of Al-Fe (20 wt%) as-cast alloy SEM micrograph of Al-Fe (20 wt%) as-cast alloy is shown in Fig. 1a.

The observed morphology consists of elongated intermetallic grains and porosities dispersed in the bulk material [16]. EDS chemical maps illustrating the elements distribution is shown in Fig. 1b. It showed the Al and Fe were distributed in two phases. In order to know the structure of both crystallographic phases, an XRD analysis was performed. Fig. 2 shows the XRD pattern that indicates the presence of the Al (Fe) cubic solid solution and $Al_{13}Fe_4$ monoclinic intermetallic compound. These results are in agreement with the Al-Fe phase equilibrium diagram.

Fig. 3 shows the potentiodynamic polarization curves for the Al-Fe (20 wt%) alloy immersed in artificial seawater at different pH values by $Ca(OH)_2$ addition. As the pH increases, the anodic and cathodic areas are displacing toward small potential values and high current density values, more accentuated at pH 14 with higher current density values. For pH 10, 12 and 14 the anodic polarization regions were associated with a mechanism of anodic dissolution at potentials near to OCP. A semi-passive region between -796 to -646 mV_{SCE} was observed at pH 10, while at pH 12 and 14 longer semi-passive region was present from -940 to -480 mV and -910 to -580 mV respectively. However, higher active dissolution was observed at pH 14. In addition, with increasing pH values the i_{corr} increased in one order of magnitude associated with the aluminium dissolution into the activation region.

For pH 10 and 12 there is a semi-passive behaviour attributed to the formation of corrosion products trapped between Fe-Al phases; retarding the ion transfer mechanism at the alloy interface as a resistive barrier. A similar behavior has noted in materials susceptible to pitting corrosion [17]. However, at pH 14 an activation mode was the principal mechanism for over potential near the OCP.

The anodic dissolution mechanism is increased with the pH values when $Ca(OH)_2$ was added (Fig.3). At pH 10, an active region was formed in the range from OCP to -891 mV showing an i_{corr} of 11.87 x10^{-3} mA/cm^2 and a semi-passive region presented at i_{pass} value around 0.1617 mA/cm^2.

Similarly, at pH 12 and 14 an active region from the OCP observed in the range -940 to -910 mV showing i_{corr} values of 37.2 x10^{-3} and 89.63 x10^{-3} mA/cm^2 respectively. Also, a semi-passive region shows i_{pass} values around 0.345 and 0.67 mA/cm^2. Instabilities showed in cathodic branches are related to the transformations in mixtures of salts at the beginning and the end of the experiment, attributed to the release of corrosion products formed on the surface of the intermetallic alloy [17, 18]. As in the present study some aluminium alloys, corrosion studies have reported changes in the Tafel slopes of the cathodic polarization curve in aqueous solutions attributed to the rupture of the oxide film formed on the cathodic surface [19, 20].

Table 1. Potentiodynamic polarization parameters for the Al-Fe (20 wt%) alloy tested in seawater at different pH values by Ca $(OH)_2$ adding.

Electrolyte (Seawater)	pH	E_{corr} mV	i_{corr} mA/cm^2	βa mV/$_{decade}$	βc mV/$_{decade}$
Seawater	8	-1114	8.0 x10^{-3}	549	465
Seawater + CaOH	10	-1045	11.8 x10^{-3}	407	350
	12	-1237	37.2 x10^{-3}	147	124
	14	-1241	89.6 x10^{-3}	112	100

Table 1 shows the electrochemical parameters obtained from potentiodynamic polarization curves, where the i_{corr} was calculated by the method of extrapolation of Tafel (βa and βc) in the range of ±150 mV vs. OCP. The increasing in current density (i_{corr}) was related to the dissolution process.

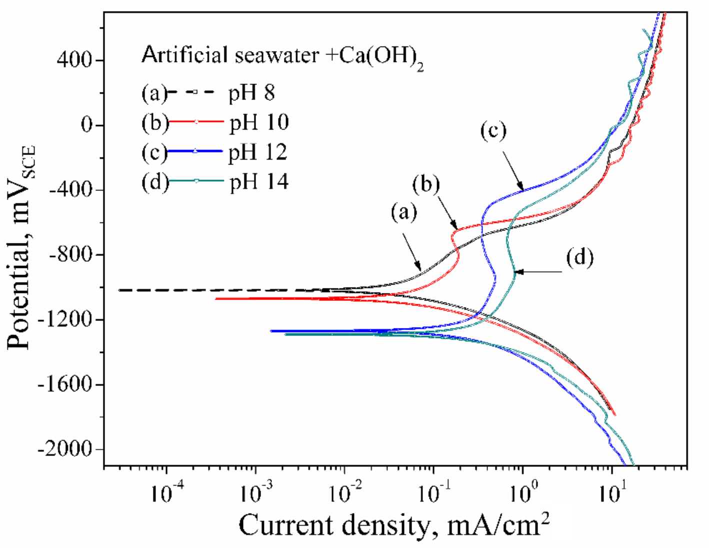

Figure 3. Potentiodynamic polarization curves for the Al-Fe (20 wt%) alloy in seawater at different pH values by $Ca(OH)_2$ adding.

The results obtained from linear polarization resistance (LPR) of the alloy immersed in seawater with the pH effect on the R_p kinetic, are showed in Fig. 4. $Ca(OH)_2$ additive decreased the R_p values in the range 0.1 to 100 kΩ cm^2 showing an increase in the corrosion rate. At pH 14, the R_p values were lower attributed to a minimum or unstable corrosion products formed with permeability characteristics, and the passivation-breaking-passivation process caused by seawater composition.

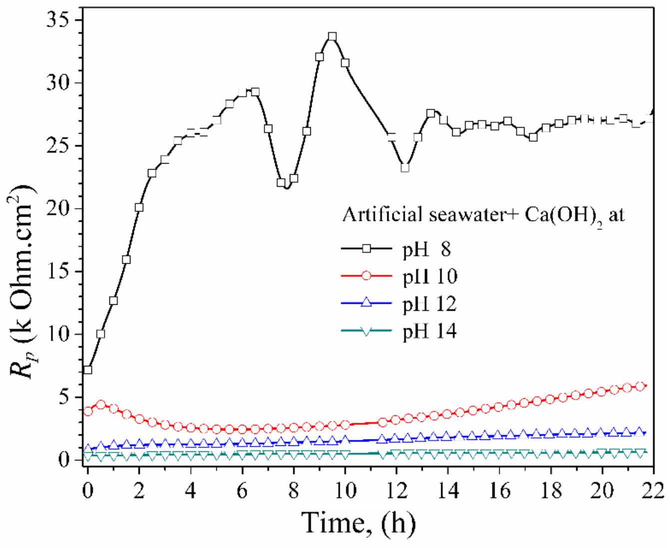

Figure 4. LPR at different pH with $Ca(OH)_2$ additions.

From potentiodynamic results, the i_{corr} of the alloy increased slightly from 8 x10^{-3} to 89 x10^{-3} mA/cm^2 with pH by the $Ca(OH)_2$ addition. This variation in current density was attributed to the instability of the hydrated γ-Al_2O_3 phase according to the aluminium Pourbaix diagram [21]. At pH 8, lower i_{corr} values of the alloy were observed, which was confirmed by the increase the values of R_p in the range from 7 to 29 kΩ cm^2 for a period ranging from 1 to 6 h. Subsequently, R_p values stay stable around the 26 kΩ cm^2 after 12 h of immersion. In the other hand, for pH>8 the solutions show values of R_p up to 5 kΩ. Notably, the alloy at pH 14 showed a maximum R_p around 0.6 kΩ cm^2 after 20 h of immersion. These results illustrate a higher anodic dissolution obtained for pH>8 promoting high density of electrochemical reactions with possibilities of produce higher hydrogen liberation. It could be usable for energy conversion in future applications.

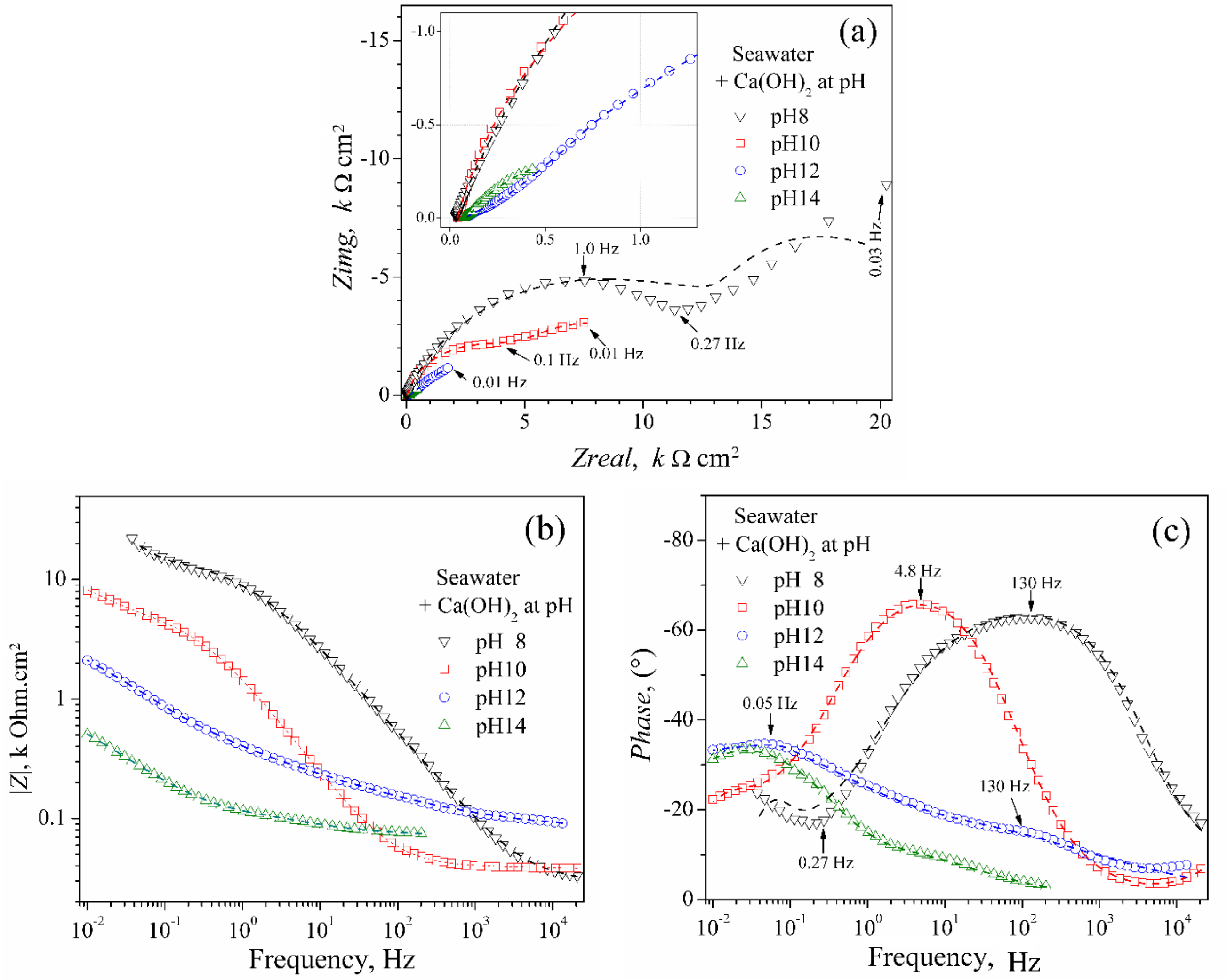

Figure 5. EIS results; a) Nyquist, b) Impedance module, c) Bode phase diagrams.

Fig. 5 shows the EIS results from the immersion of Al-Fe (20 wt%) alloy in seawater at different pH values by adding $Ca(OH)_2$. Fig. 5a is illustrating the Nyquist diagrams. At pH 8 (near to neutral seawater), a depressed capacitive semicircle situated from higher to middle frequencies (up to

0.27 Hz) is observed due to the initial surface rough which increased with the anodic dissolution. At pH 10, a capacitive semicircle from high to medium frequencies (up to 0.1 Hz), tending to form a second semicircle at lower frequencies was presented. Nyquist diagrams for pH 12 and 14 show low frequencies and a second opened semicircle with diffusive behavior due to the formation of corrosion products which added to alloy surface. The formation of second opened semicircles was related to the presence of a permeable layer rapidly dissolved at pH>8. The decrease in semicircle diameter at pH 12 and 14 suggest an increase in the current density indicating both formation of stable corrosion products and a process of charge transfer. These results are in good agreement with the polarization curves at low overpotential close to the OCP (Fig. 3). Fig. 5b illustrates at low frequencies the maximum value of impedance module |Z| reaching 20 kΩ cm^2 at pH 8. The impedance module for a frequency of 0.01 Hz was approximately 8.1 kΩ cm^2 at pH 8 and 10 defining time constants. These results are in agreement with the Nyquist diagrams at the same pH values. The minimum values of the impedance module registered at low frequencies (pH>8) were approximately the same with R_p (see Fig.4). The phase angle determined at high frequencies shows low values related to electrolytic reactions governed by an activation mechanism. At pH 8 and 10, the phase angle is increased at low-frequency values indicating higher stabilities of the corrosion products. This trend is similar to the LPR results showed in Fig. 4.

The hydrogen evolution during the electrochemical process [22] correspond to the hydration-dissolution and precipitation of aluminium corrosion products formed at the surface/electrolyte surface promoted by the pH increasing and uncovered substrate sites by the scale spalling [22]. That maintains a constant effective area in contact with the alkaline solution, as showed with EIS results of alloys in both pH 12 and pH 14 solutions. In this sense, the equivalent circuit model (ECM) in Fig. 6 shows analogous representation with electric elements of the corrosion phenomena mechanisms, considering the formation of the porous and defective scale of corrosion products. In the ECM, R_s is the resistance of the electrolyte solution, the arrangement of CPE_1 in parallel with R_p is the impedance of the external scale/solution interface. The element CPE_2 is the double layer capacitance between metal and electrolyte solution at the pore bottom, as before reported [23]. The R_{CL} is the charge transfer resistance at the alloy surface and the electrolyte into the pore.

The schematic corrosion products porous scale (Fig. 6) allows the electrochemical reactions at the exposed electrode surface due electrolyte permeation. However, in the kinetic model, the electrochemical reactions into the pore could differ from the bulk interface due the differential species concentration. At the bottom pore interfaces, the corresponding impedance was composed by an R_{cl} $+W_s$ in parallel with CPE_{2l} (the double-layer capacitance at the metal/solution interface) electrical component arrangement. Inside the pore length interface, the electrolyte resistance R_p, and the impedance in the pore are in parallel with the insulating part of the inner scale; it considered as a capacitor CPE_1 [24,25]. [24,25]. Table 2 shows the EIS parameters fitted over the data values obtained during the Al-Fe (20 wt%) alloy immersion into the seawater solution at different alkaline pH conditions, using the two equivalent electrical circuit models showed in Fig 6.

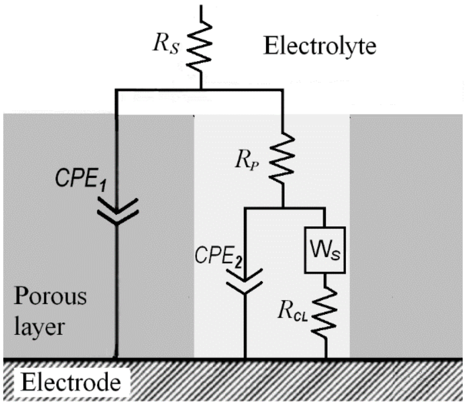

Figure 6. Equivalent electrical circuit of the impedance for an electrode with porously corrosion product formation by the Al-Fe (20 wt%) alloys immersed in seawater at different pH values.

$$Z_{(CPE)} = \frac{1}{T_{CPE}(j\omega)^{\alpha}} \tag{2}$$

$$Z_{(R)} = R_S \tag{3}$$

$$Z_f = R_{CL} \tag{4}$$

$$Z_W = \sigma \frac{\tanh(jT_D\omega)^P}{(jT_D\omega)^P} \tag{5}$$

Were:

R_s is the electrolyte resistance, T_{CPE} is a constant phase capacitance, α dimensionless potential number ($0 < \alpha \le 1$; while $\alpha=1$ assumes CPE_i is a perfect capacitance C_{dl}). Angular frequency is $\omega = 2\pi f$, with f = *linear frequency*, j a complex number $= \sqrt{-1}$, and Z_f is the Faradaic impedance at the metal/scale interface. Hence, the term T_D represents the ratio of scale thickness L and the effective diffusion coefficient D_{eff} of that scale; $T_D = L^2 D_{eff}^{-1}$, power is between $0 < P < 1$, $\boldsymbol{\sigma}$ is the constant of diffusion or the modulus of the *Warburg* resistance.

Table 2. EIS obtained fitting parameter by ECM (Fig. 6) of measured data obtained with the Al-Fe (20 wt%) alloys immersed in seawater at different pH values.

Seawater + $Ca(OH)_2$	pH 8	pH 10	pH 12	pH 14
R_s, (Ω cm^2)	24.12	2.12 x10^{-7}	78.61	71.26
T_{CPE1}, (F cm^2)	1.59 x10^{-5}	7.68 x10^{-8}	1.05 x10^{-3}	3.54 x10^{-3}
α_1, dimensionless	0.69	0.89	0.36	0.56
R_p, (Ω cm^2)	20.39	39.11	580.2	76.19
T_{CPE2}, (F cm^2)	1.76 x10^{-6}	1.29 x10^{-4}	4.85 x10^{-4}	4.15 x10^{-3}
α_1, dimensionless	0.90	0.84	0.62	0.91
$\boldsymbol{\sigma}$, (Ω cm^2/s)	8905	7254	27799	1204
$\boldsymbol{T_D}$, (s)	6.273	48.5	6.057	106.5
$\boldsymbol{P}$, dimensionless	0.620	0.440	0.698	0.304
$\boldsymbol{R_{CL}}$, (Ω cm^2)	14529	4218	3499	1.5 x10^{-4}

In accord with the EIS and fitting results, the R_s values were minor than 80 Ω cm^2. R_{CL} values showed in agreement with the R_p from LPR monuments, were the alloy immersed in the solution at pH 14 showed the lowest values while at pH 8, the highest value was observed. Warburg elements showed lower values, which are associated to more diffusivity between the defective scales of corrosion products, were ionic diffusion found high-density paths across the scale, Table 2. In this sense, defective corrosion product affected the surface area of scale/electrolyte interface; it was associated with the potency factor (α_1) of the capacitive constant element CPE_1, showing in all cases, α_1 values under of 0.9, particularly at both 12 and 14 pH values around 0.5. The last characteristic promoted a semicircle depreciation explained by Nyquist plots (Fig.5a). On the other hand, the capacitive element at the alloy/scale/pore interface, showed α_2 values closer to 0.9, tending to get perfect capacitance behavior.

The fitting parameter of ECM proposed is in accord with the electrochemical experimental results and with the microstructural characterization of surface alloys after the corrosion tests. The capacitance values increased with the pH for the two constant elements (CPE), due its impedance (Z_{CPE}) values diminished and scale density fall also, as discussed before [26]. Last behavior was promoted by the $Ca(OH)_2$ addition in seawater solution.

Fig. 7 shows XRD patterns of the sample at pH 8 and 14 exposed to seawater with $Ca(OH)_2$ addition. For sample at pH 8, the same starting phases were observed indicating a weak or not alloy reaction with seawater. By contrast, in the pattern at pH 14, the $Na_2Ca(CO_3)_2 \cdot 5H_2O$ phase and minor proportions of NaCl compound observed as constituents of seawater are indicating the effect of the pH in the alloy corrosion.

Fig. 8 displays surface images of the alloy exposed to seawater at pH 14. A visible dissolution of the alloy was observed. The aluminium oxide is thermodynamically stable near neutral seawater, showing excellent adhesion to the substrate. Therefore, the aluminium oxide layer is an ideal protective layer [27]. However, the layer can be dissolved in alkaline solution as can be deduced in the present work.

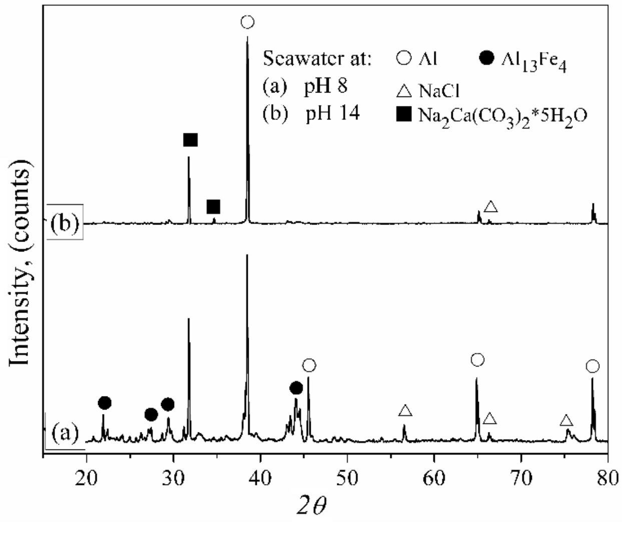

Figure 7. X-Ray diffraction pattern in corroded condition at different pH with $Ca(OH)_2$.

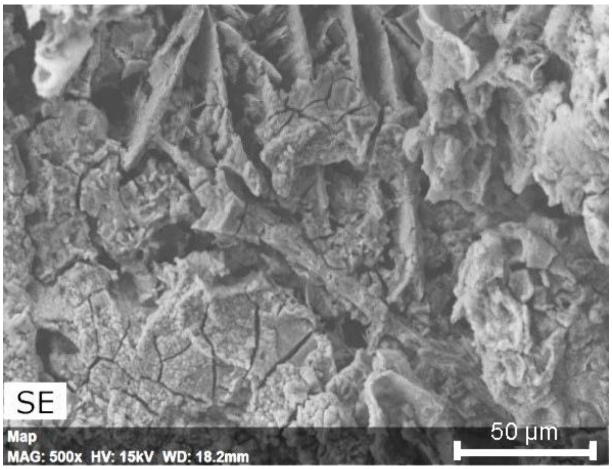

Figure 8. SEM micrograph showing characteristics on the corroded surface of alloy immersed in seawater solution at pH 14.

4. CONCLUSIONS

After the corrosion test on the Al-Fe (20 wt%) alloy immersed in seawater at pH 10, 12 and 14 by $Ca(OH)_2$ additions, the following conclusions are derivate:

The potentiodynamic plots show anodic dissolution and semi-passive behaviour at higher potential values from OCP. With pH increasing the alloy shows higher i_{corr} values.

EIS results from the Nyquist plots with the pH increasing show a semicircle diameter reduction as an indication of the impedance module values are associated to charge transfer control governed by a corrosion mechanism.

The electrochemical properties modified a semi-passive layer forming a defective scale with porous high density accentuated by $Ca(OH)_2$ addition. In this sense, the R_p values of the alloy decreased with pH.

XRD patterns showed the presence of the $Na_2Ca(CO_3)_2 \cdot 5H_2O$ and NaCl compounds identified as constituents of seawater in the alloy. SEM images indicate the formation of stable surface layers that obstruct and slow the corrosion process. The film growth was due to the ionic migration of Al^{3+} and O^{2-} through the film thickness, indicating greater dissolution of the alloy by $Ca(OH)_2$.

ACKNOWLEDGEMENTS
J.E. Flores-Chan expresses their gratitude to PRODEP for the financial support granted for the development of this research.

References

1. J. R. Romero-Romero, J. Luis López Miranda, R. Esparza, M.A. Espinosa-Medina and G. Rosas, *Mater. Sci. Forum*, 793 (2014) 143-149

2. H. Song, Y. Wu, C. A. Tang, S. Yuan, Q. Gong, and J. Liang, *Tsinghua Sci. Technol.*, 14 (2009) 300-306
3. Ji. Gang, T. Grosdidier, F. Bernard, P. Sebastien, E. Gaffet and L. Sebastien, *J. Alloys Comds*, 434 (2007) 358-36
4. O. Hernández, F. de la Rosa, A. Bedolla, C. Patiño-Carachure and G. Rosas, *Superficies y vacío,* 26 (2013) 18-21
5. M. Martinez, B. Viguier, P. Maugis, J. Lacaze, *Intermetallics* 14 (2006) 1214-1220
6. C. T. Liu, Mater. Chem. Phys. 42 (1995) 77-86
7. R. Akid, Corrosion of Engineering Materials, Handbook of Advanced Materials, Wiley inter-science, United States of America 2004
8. Y. K. Chen, H. T. Teng, T. Y. Lee, H. W. Wang, Int. J. Energy Env. Eng., 5 (2014) 1-6
9. M. Pudukudy, Z. Yaakob, B. Narayanan, R. Ramakrishnan, S. Viswanathan, Int. J. Hydrogen Energy, 37 (2012) 7451-7456.
10. E. A. EI-Wahab, A. H. Marei, O. R. Khalifa, H. A. Mohamed, *J. Am. Sci.,* 6 (2010) 476-486
11. A. Aballe, M. Bethencourt, F. J. Botana, M. Marcos, J. Pérez-Mariscal, *Rev. Metal.*, 34 (1998) 37-41
12. A. A. El-Meligi, International Journal of Hydrogen Energy 36 (2011) 10600-10607
13. L. Soler, A. M. Candela, J. Macanás, M. Muños, J. Casado, *J. Power Sources,* 192 (2009) 21-26.
14. H. Z. Wang, D. Y. C. Leung, M. K. H. Leung, M. Ni, *Renew. Sust. Energ. Rev.*, 13 (2009) 845-853
15. C. B. Porciúncula, N. R. Marcilio, I. C. Tessaro, M. Gerchmann, *Braz. J. Chem. Eng.*, 29 (2012) 337-348
16. W. John Pridgeon, L EdwardLanger, ASM Handbook, Vol. 9, Metallography and Microstructures, 9th Edition, Printed in the United States of America, 2004
17. W. J. Lee, S. I. Pyun, Electrochim. Acta 45 (2000) 1901-1910
18. L. Martinez, M. Amaya, J. Porcayo-Calderon, E. J. Lavernia, *Mater. Sci. Eng., A,* 258 (1998) 306-312
19. M. Amaya, M.A. Espinosa-Medina, J. Porcayo-Calderon, L. Martinez, J. G. Gonzalez-Rodríguez, *Mater. Sci. Eng., A,* 349 (2003) 12-19
20. K. Nisancioglu, H. Holtan, *Electrochim. Acta* 24 (1979) 1229-1235
21. M.Pourbaix, Aluminium Atlas of Electrochemical Equilibrium in Aqueous Solutions, Ed Pergamon, Oxford. 1966.
22. V. Sarou-Kanian, S. Ouazar, P. E. Bocanegra, C. Chauveau, I. Gokalp, Low temperature reactivity of aluminum nanopowders with liquid water, In Proceedings of the 3rd European Combustion Meeting ECM.
23. C. L. Zeng, W. Wang, W. T Wu, *Corrosion Sci.*, 43 (2001) 787-801
24. N.J. Medvedeva, Y.N. Gornostyrev, D.L. Novikov, O.N. Myrasov and A.J. Freeman, *Acta Mater.* 46 (1998) 3433-3442.
25. Y. L. Zhou, M. Ninomi, T. Akahori, H. Fukui and H. Toda, *Mater. Sci. Eng., A*, 398 (2005) 28-36.
26. J. R. Macdonald, E. Barsoukov, Impedance spectroscopy: theory, experiment, and applications. John Wiley and Sons, New Jersey, 2005.
27. F. Rosalbino, S. Delsante, G. Borzone, E. Angeline, *Corrosion Sci.*, 52 (2010) 322-326.